CYCLIC RESPONSE OF PRECAST COLUMN-TO-FOUNDATION CONNECTION USING UHPC AND Ni-Ti SMA REINFORCEMENTS IN COLUMNS

Pereiro-Barceló, Javier[1]**; Bonet, José L.**[2]; **Rueda-García, Lisbel** [3]**; Albiol-Ibáñez, José Ramón** [4]

[1] Departamento de Ingeniería Civil (DIC), Universidad de Alicante, San Vicente del Raspeig, Carretera San Vicente del Raspeig unnumbered, Alicante, 46022, Spain javier.pereiro@ua.es

[2] Instituto Universitario de Ciencia y Tecnología del Hormigón (ICITECH), Universitat Politècnica de València, Valencia, Spain C/Vera unnumbered, Valencia, 46022, Spain jlbonet@cst.upv.es

[3] Instituto Universitario de Ciencia y Tecnología del Hormigón (ICITECH), Universitat Politècnica de València, Valencia, Spain C/Vera unnumbered, Valencia, 46022, Spain lisruega@cam.upv.es

[4] DCAR (Architectonic Constructions Department), Universitat Politècnica de València, Valencia, Spain C/Vera unnumbered, Valencia, 46022, Spain joalib1@csa.upv.es

ABSTRACT

Earthquakes are catastrophic natural events with a special impact on reinforced concrete structures due to the horizontal loads that they introduce into structures. To adequately resist an earthquake, a precast structure must have a high deformation capacity, dissipate energy in each earthquake cycle, undergo less damage and fewer residual deformations. To achieve all this, the behaviour of precast columns made with UPHC was herein experimentally analysed. Steel rebars were replaced with Ni-Ti shape memory alloy (SMA) bars with superelasticity (SE) in the critical zone of the column-to-foundation connection. The Ni-Ti SMA bars crossed the interface between the column and foundation. Two types of connection with the foundation were studied: smooth pocket type and protruding bar type. Columns were subjected to constant compression and a cyclic lateral load. Rocking behaviour was observed at the connection critical section. The use of advanced materials allowed a moment-rotation behaviour of the connection to be developed without any significant damage. Low residual deformations were observed while testing because of both the damage in UHPC was low and the superelasticity of the Ni-Ti SMA bars.

Keywords: UHPC, Ni-Ti, SMA, self-centering, cyclic load, ductility, residual drift ratio.

HIGHLIGHTS:

- Four precast column-to-foundation connections with UHPC and Ni-Ti SMA were tested
- The influence of the column-to-foundation connection type was studied
- Cyclic response of precast columns was studied
- High ductility was reached thanks to smarts materials

1. Introduction.

Earthquakes are catastrophic natural events with a special impact on reinforced concrete structures due to the horizontal loads that they introduce into structures. The behaviour of precast reinforced concrete structures in seismic areas depends, among other factors, on the type of joint linking the different precast elements into which the structure is divided. Precast structures (industrial buildings, commercial buildings, car parks) are generally projected with pinned joints and base-fixed columns. Precast bridge piers are normally designed so that the hinge appears in this element, which must be fixed or pinned with the deck. The first-floor columns of precast buildings are designed in such a way that a plastic hinge is produced in the fixity. Therefore, it is necessary for such columns to be capable of providing an inelastic response without no capacity loss [1,2]. That is, the plastic hinges that form in columns need great rotation capacity, while maintaining the bearing load. These columns' deformation capacity depends on the combined behaviour of the column and the column-to-foundation connection. Furthermore, it is desirable that this deformation capacity is associated with high energy dissipation to mitigate earthquake effects. It is also desirable that the damage that construction suffered during an earthquake is as little as possible, and the same can be stated of the drift and residual deformations after the seismic event, because repair costs can be very high even though the structure did not collapse during the earthquake. Therefore, for a precast structure to adequately resist an earthquake, it must have a great deformation capacity, dissipate energy in each earthquake cycle and undergo less damage and fewer residual deformations.

In accordance with design codes like EC-8 [1], ACI-318-19 [3], EHE-08 [4] and NCSP-07 [5], high deformation capacity can be achieved with a high transverse reinforcement ratio where plastic hinges form. The problem with this solution is that pouring concrete into columns can be difficult given the high transverse reinforcement ratio arranged. For this reason, several authors [6–11] have replaced part of transverse reinforcement with steel fibres in the concrete composition. These authors indicate that the addition of fibres improves the deformation capacity and energy dissipation and reduces damage.

Normally in a precast reinforced concrete structure, energy dissipation is achieved by causing damage to materials (concrete cover spalling, concrete crushing, reinforcement yielding) [12]. Consequently, residual deformations are high [12]. Therefore, with conventional materials, it is not possible to design precast structures with high deformation and strength capacity, keeping high energy dissipation, and reduced damage and residual deformations [12]. This is why the present study uses advanced materials like Ultra High-Performance Concrete (UHPC) and Nickel and Titanium (Ni-Ti) Shape Memory Alloy (SMA) bars with superelasticity in the connection between the column and the foundation.

On the one hand, UHPC is a cementitious composite material with a high metallic fibre content (from 1% in volume) [13], a 28-day compressive strength of at least 120 MPa [14,15] and up to 45 MPa of flexural tensile strength [16,17]. Its high fibre content and its bond to these fibres due to its high compressive strength confer reinforced concrete elements great ductility without having to increase the transverse reinforcement ratio [16,18–26]. Furthermore, UHPC undergoes less damage than other concretes under equal conditions [22,27,28] and greater energy dissipation capacity [23]. This material is also being used in the precast construction field [27,29,30].

On the other hand, SMA bars are materials whose behaviour is very ductile (reaching stress of 950 MPa for a strain of 45%) and are capable of reaching a high strain level and returning to a predefined shape after unloading or heating. In structural engineering terms, they have three key properties: shape memory effect (SME), superelasticity and damping capacity. The SME refers to the material's ability to return to a predefined shape after heating, while superelasticity is the phenomenon that allows its original shape to recover after an unloading process. Finally, damping capacity is a property linked with the other two, which allows the structure movements and vibrations to be reduced thanks to mechanical energy conversion into thermal energy. All these characteristic properties of SMA bars are the result of the reversible transformation phase that these materials undergo, which is called martensitic transformation. Replacing steel bars with Ni-Ti SMA bars in structural members' critical areas where plastic hinges will be formed can improve member ductility [31–40], energy dissipation [41,42] and the reduction of residual deformations due to its superelasticity [41–45]. Ni-Ti is the most widely used alloy [31–36], although other types exist like Fe-based SMAs [46–49] or Cu-based SMAs [38,39,50–52].

The combination of NiTi-SMA and UHPC reinforcements causes small residual deformations to the structure and also causes the concrete can withstand the large strains that NiTi can experience, both in compression and in tension. Critical sections can develop a large curvature that can be supported by both concrete and NiTi SMA without undergoing excessively damage which produce large residual strains [2]. In a previous investigation carried out by Pereiro-Barceló et al. [2] the beam-column connection made in-situ was tested with specimens entirely fabricated with High Performance Concrete HPC (compressive strength of 80 MPa and a fibre content of 1% in volume) and others entirely fabricated with UHPC. All longitudinal reinforcement in beam-column connection were SMA bars. The results were that HPC could not withstand the large strains that are necessary for SMA to develop considerable stresses due to its low elasticity modulus (60 GPa). The dissipation energy of SMA-UHPC structure is higher than conventional material structure even though the superelastic NiTi develop small residual strains. This is due to the fact that, in SMA-UHPC specimens, critical section curvature is higher and, consequently, the strains reached by the materials are higher [2] and because UHPC can dissipate a large amount of energy due to its ductility and its strength capacity [2].

For all these reasons, the behaviour of the precast column-to-foundation connection was experimentally analysed in this paper, where the column was fabricated with UPHC, and the conventional steel bars were replaced with Ni-Ti SMA bars in the connection area. The objective of the article is to minimize the damage and residual deformations in the column-foundation connection, maintaining an adequate strength, deformation and energy dissipation capacity. Two types of connection with the foundation have been studied: smooth pocket (from now on SP) and protruding bar (from now on PB). Columns were subjected to constant compression and a cyclic lateral load. Other connection types such as rough pocket connection or bolted socket connection were not studied in this research because, according to Romero-García et al. [1], constructive procedure of SP is easier and strength capacity of RP connection were lesser than the SP connection. BS connection was not studied because is a more complex connection that should be studied in a second phase not to add more variables to the analysis.

2. Experimental programme.

2.1. Specimens

Four columns of a 260x260 mm square section and 2000 mm long were fabricated and tested in a horizontal position; see Figure 1. The shear slenderness λ_V of all the columns equalled 7.69 ($\lambda_V = L_s/h = M/(V \cdot h)$, where *h* is the cross-section depth, *M* and *V* are the applied bending moment and shear force, respectively, and L_s is column length). The results of this paper are valid for this slenderness. A greater number of tests would be necessary to obtain relevant conclusions. Second-order effects cannot be neglected. Nevertheless, code EC-8 [1] can be applied to those columns with shear slenderness below 10. Each column was embedded in a foundation element that was 830x760x660 mm in size. That foundation element was connected to a test frame by a 470-mm long metal element. The whole assembly was pinned-pinned, and the total specimen length was 3300 mm. The specimens were tested up to a 5% drift ratio where most of the specimen exhibited at least 20% lateral load loss.

The behaviour of the SP and PB connections were studied. With the SP connection, the column was embedded in the foundation for a length that equalled 520 mm, twice the column's depth. In this connection, and in order to generate the hole in the foundation, a smooth metal pyramid-shaped formwork providing 100 mm of tolerance in each direction to insert the column was used. This space was filled with expansive mortar (Sika Grout®-213) once the precast column had been placed and levelled. To the protruding bars connection, longitudinal bars were anchored inside a 65-mm diameter sleeve with a 700-mm anchorage length. Sleeves were filled with expansive mortar (SikaGrout®-213). In order to ensure contact between the upper face of the foundation and the column base, an epoxy resin construction adhesive (Sikadur®-52) was applied. The connection of the precast column with the foundation was made 10 days before the test.

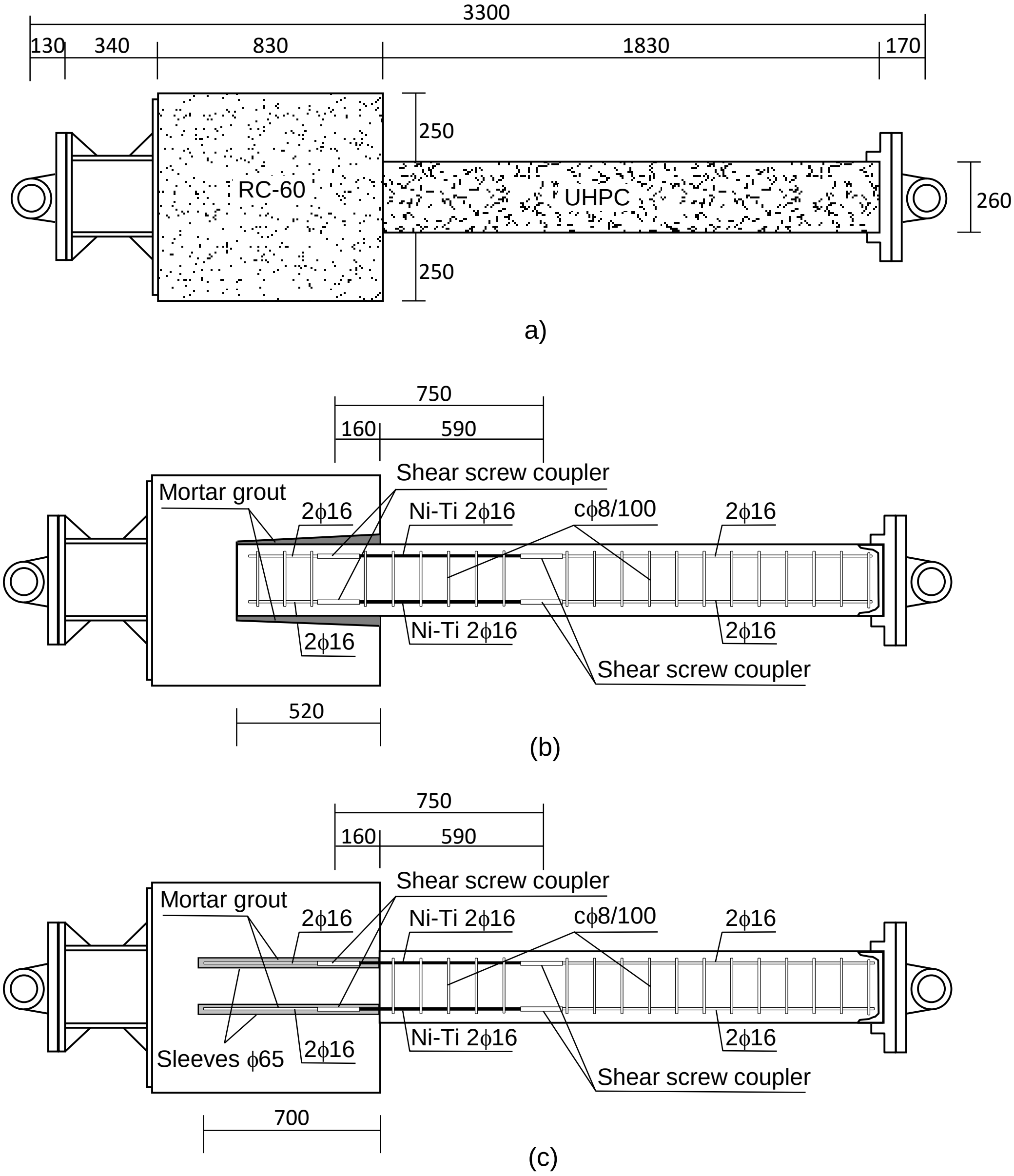

Figure 1: Dimensions and reinforcement of the test specimen (unit: mm) (a) dimensions; (b) smooth pocket; (c) protruding bars.

A constant longitudinal reinforcement was arranged along the entire column, consisting of four 16-mm diameter bars in each corner (Figure 2). This gave a longitudinal reinforcement ratio (ρ_l) of 1.19%. Steel bars were replaced by Ni-Ti shape memory alloy bars (Ni-Ti SMA) with superelasticity at a length that equalled 590 mm from the interface between the column and the foundation in the critical zone of the connection (Figure 1.b and c). This length was similar to the column critical length of 600 mm, according to EC-8 [1] for a high ductility class (DCH). The Ni-Ti SMA bars crossed the joint between the column and the foundation insofar as at least 160 mm of the bar entered the foundation. The total Ni-Ti SMA bar length was 750 mm. Clamping screw couplers were used to join the steel and Ni-Ti reinforcements. Three screws, designed to break at a given torque, were employed to tighten the bars. This connection was designed according to Bonet et al. [32].

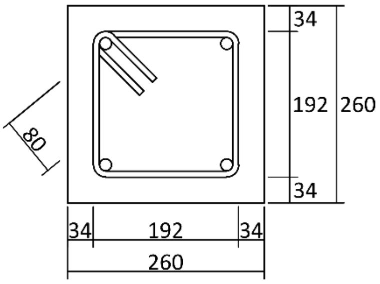

Figure 2: Cross-section details (unit: mm).

The transverse reinforcement was an 8-mm diameter stirrup separated every 100 mm (cØ8/100), which corresponded to a geometric transverse reinforcement ratio (ρ_w) of 1.09%. Transverse reinforcement spacing equalled 6.25·*D*, where *D* is the longitudinal reinforcement diameter that equalled 16 mm. This spacing was slightly wider than the maximum spacing recommended to avoid local buckling the longitudinal reinforcement in concrete elements fabricated without steel fibres in their mass, as proposed by ACI-318-19 [3] (6·*D* for ordinary structures, and 5·*D* for special structures for Grade 80 longitudinal bars, which corresponds to a similar yield strength of the employed steel bars), and by EC-8 [1] for high ductility (DCH) equalling 6·*D*. These recommendations do not take into account the favourable effect of using steel fibres on the concrete mass [10,11,41,53,54]. All the stirrups were anchored with 135º bends extending 80 mm (10·ϕ_t where ϕ_t is the nominal diameter of the stirrup) into the concrete cover. This length meets the requirements of EC-2 [55] (5·ϕ_t > 50 mm) and ACI-318-19 [3] (6·ϕ_t > 50 mm), the minimum length reported in ACI-318-19 [3] for seismic actions (75 mm) and that reported in EC-8 [1] (10·ϕ_t > 80 mm).

A relative normal force ($\nu = N/(b^2 \cdot f_c)$ (where *N* is the applied axial load, *b* is the cross-section width, and f_c is the average concrete compressive strength of the column) of 0.20 was applied in all the tests. Therefore, the results of this research are just valid for this relative axial force. The minimum value to consider the structural element as a column is 0.10 (EC-8 [1] and ACI-318-19 [3]). The selected relative normal force was conditioned by the hydraulic actuator and was lower than the upper limits contemplated in EC-8 [1]: 0.65 for a medium ductility class (DCM) or 0.55 for a high ductility class (DCH).

Table 1 details the four specimens included in the experimental programme. This table provides the age of the specimen since the precast column was fabricated. Designation of the specimens was carried out using Zx-YYV02, where "x" indicates the specimen number and "YY" the connection type (PB for protruding bars and SP for smooth pocket). For each axial load level, two specimens were tested per connection type to analyse the dispersion of the experimental results.

Table 1: Details of the test specimens

Id Specimen	Age at testing (since the precast column was built), days	b (mm)	h (mm)	λ_V	s_t (mm)	Connection type	Axial load (kN)	ν
Z1-PBV02	33	260	260	7.69	100	Protruding bars	1627.81	0.20
Z2-PBV02	27	260	260	7.69	100	Protruding bars	1710.28	0.20
Z3-SPV02	28	260	260	7.69	100	Smooth pocket	1646.74	0.20
Z4-SPV02	30	260	260	7.69	100	Smooth pocket	1644.30	0.20

2.2. Material characterisation.

To fabricate each specimen, two concrete types were used (Figure 1.a). One concrete had a nominal compressive strength of 60 MPa (RC-60), and was used in the foundations. In the columns, an ultra-high performance concrete (UHPC) with a high fibre content was employed, composed of short (13 mm long) and long (30 mm long) fibres to ensure good service and failure performance. The fibre content in UPHC was 150 kg/m^3, which corresponded to a volumetric steel/fibre ratio of 1.9%. The nominal compressive strength of UHPC was 120 MPa. Table 2 indicates the UHPC dose.

The steel fibres used for UHPC were: DRAMIX® RC-80/30 BP which have a hook end, are 30 mm long with a slenderness of 80, a yield strength of 3070 MPa and modulus of elasticity of 200 GPa; DRAMIX® OL-13/0.16 with a straight geometry that is 13 mm long with a slenderness of 81.25, a yield strength of 2750 MPa and a modulus of elasticity of 200 GPa.

Table 2: Concrete dose (kg/m³).

Description	UHPC
Cement I 42.5 R	1000
Water	177
Sand (D_{max} 0.8mm) AF_T_0/8_S	575
Sand (D_{max} 0.4mm) AF_T_0/4_S	310
Silica fume	150
Steel fibres DRAMIX RC-80/30 BP	60
Steel fibres DRAMIX OL-13/0.16	90
Super-plasticiser	29

** D_{max}: Maximum aggregate size

The results of the characterisation of the concretes used in both the foundation (RC-60) and the column (UHPC) are shown in Table 3, where f_c is the average concrete compressive strength and E_c is the concrete's modulus of elasticity. These properties were measured according to the indications set out in UNE-EN 12390-3:2020 [56] and UNE-EN 12390-13:2014 [57]. For both concrete types, a sample of four concrete cylinders (300 mm high, 150 mm diameter) was taken. Table 3 shows the results of the flexural tensile strength test done with UHPC according to Standard UNE EN 14651:2007 [58] (measured on 550x150x500 mm prisms), where f_{LOP} is the limit of proportionality and $f_{R,j}$ (for j = 1-3) corresponds to the crack mouth opening displacement (CMOD) of 0.5, 1.5 and 2.5 mm, respectively. Finally, Table 3 indicates the average compressive strength of the grout mortar according to UNE-EN 12390-3:2020 [56], used in the connection between the column and the foundation (Figure 1.b and c). In this case, four concrete cubes (100 mm side) were taken. The characterisation tests of the materials were carried out on the same day as the specimen was tested.

Table 3: Mechanical properties of the test specimen concretes.

Id Specimen	Foundation		Column						Mortar grout
	f_c (MPa)	E_c (MPa)	f_c (MPa)	E_c (MPa)	f_{LOP} (MPa)	f_{R1} (MPa)	f_{R2} (MPa)	f_{R3} (MPa)	f_c (*) (MPa)
Z1-PBV02	70.35	41746	120.4	42256	14.03	23.12	22.03	19.25	53.02
Z2-PBV02	48.51	39785	126.5	46519	10.15	17.71	16.87	13.82	52.56
Z3-SPV02	67.09	39675	121.8	42506	14.19	25.01	26.98	22.79	51.92
Z4-SPV02	61.03	39560	121.6	42324	12.25	21.34	21.46	18.33	52.04

(*) Concrete cube 100x100x100 mm

The employed steel was B 500 SD (EHE-08 [4]) and C class (EC-2 [55]). Figure 3 shows the stress-strain curve corresponding to the characterisation of steel reinforcements according to UNE-EN 10002:1:2002 [59]. In this figure, f_y, ε_y, f_{sh}, ε_{sh}, f_u, ε_u and E_s, are the yield strength of the reinforcement, the reinforcement strain at the yield strength, the stress at which the hardening branch begins, the strain associated with f_{sh}, the tensile strength of reinforcement, the strain associated with tensile strength and the modulus of elasticity, respectively. The shown values are the average of two characterisation tests run for each bar diameter.

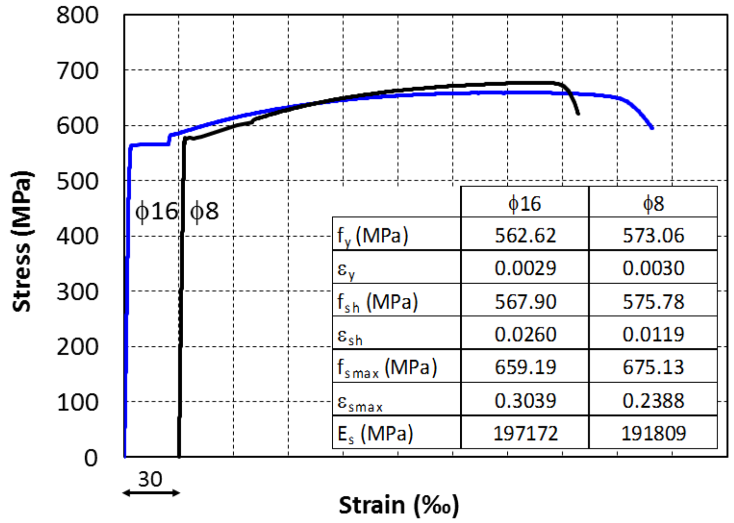

Figure 3: Mechanical properties of reinforcements.

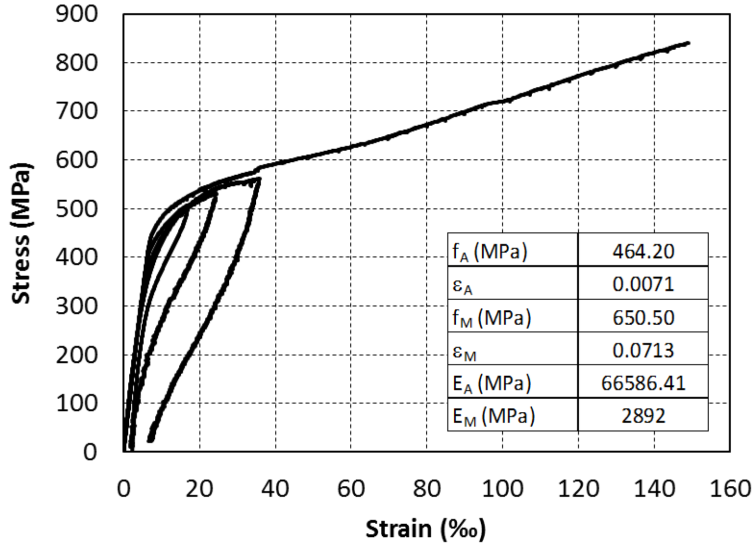

Figure 4: Mechanical properties of SMA bars.

The Ni-Ti SMA bars were 16 mm in diameter with a polished surface. By means of the differential scanning calorimetry DSC test, the four transformation temperatures were determined (A_s and A_f

for the beginning and end of austenitic transformation, M_s and M_f for the beginning and end of martensitic transformation) according to Standard ASTM F2004-05 (2010) [60]: M_f = -53.74°C, M_s = -28.47°C, A_s = -27.99°C and A_f = -5.34°C. Figure 4 depicts the stress-strain curve corresponding to the tensile Ni-Ti SMA bars testing. The austenitic modulus E_A equalled 66586.41 MPa, the martensitic modulus E_M was 2892 MPa, the martensitic transformation initial stress f_A was 464.20 MPa for a strain ε_A of 7.1‰, and the martensitic transformation end stress f_M was 650.50 MPa for a strain ε_M of 71.3‰. The test room temperature was set at 20-25°C.

2.3. Manufacturing the specimens.

Firstly, Ni-Ti SMA bars were linked with steel bars by means of screw couplers (Figure 5.a). Then, stirrups were tied to form the reinforcement specimen arrangement (Figure 5.b). In case of PB connection specimens, stirrups were not arranged to the end of longitudinal reinforcements (Figure 5.b) and they were in case of SP connection specimens (Figure 5.c). Next, reinforcements were inserted horizontally into an externally-vibrated formwork (Figure 5.d). In case of PB connection specimens, protruding bars stuck out the formwork (Figure 5.e). These columns were kept horizontal in a humid environment to minimise shrinkage effects. Once the reinforcement was set into the formwork, UHPC was made and casted (Figure 5.f and Figure 5.g). Previously, the foundation was manufactured in vertical position. The reinforcement arrangement of foundation is shown in Figure 5.h and the foundation for PB connection specimens is displayed in Figure 5.i. After three weeks from the fabrication of each column, the connection between the column and foundation was made in vertical position (Figure 5.j for PB connection specimens and Figure 5.k for SB connection specimens). Ni-Ti SMA bars crossed the column-foundation joint in both connections' types. In case of PB connection specimens, the protruding bars were inserted into the sleeves (Figure 5.l). Previously the sleeves were filled with UHPC mortar and epoxy resin was applied to column-foundation interface (Figure 5.l). In case of SP connection specimens, the tolerance gap between the column and the foundation was filled with UHPC mortar (Figure 5.m). Once mortar hardening was concluded (Figure 5.n), the specimen was turned horizontally and set into the loading frame because, approximately 28 days after manufacturing the column, test was carried out by placing the specimen in a horizontal position.

Figure 5: Manufacturing the specimens: (a) PB connection specimen reinforcement arrangement; (b) SP connection specimen reinforcement arrangement; (c) NiTi SMA – steel coupler; (d) reinforcements into formwork; (e) protruding bars sticking out of the formwork; (f) casting UHPC; (g) concrete casting concluded;

(h) foundation reinforcement arrangement; (i) foundation for PB connection specimens; (j) inserting PB connection column into foundation; (k) inserting protruding bars into sleeves; (l) inserting SP connection column into foundation; (m) UHPC mortar between the foundation and the smooth pocket; (n) finished specimen; (o) specimen turned horizontally to be inserted into the loading frame.

2.4. Test setup.

A steel-loading frame was designed to perform the tests, as shown in Figure 6.a. The horizontal loading system comprised a 2500 kN hydraulic actuator (Figure 6.b). The lateral loading system was fixed to an auxiliary frame that transmitted lateral loads to the test slab (Figure 6.c). The lateral load was applied to the specimen by a 500 kN double effect hydraulic jack. The forces applied by hydraulic actuators were controlled by two load cells: a 2000 kN cell, attached to a plate inside the horizontal loading system frame, and a 500 kN cell, between the specimen and the hydraulic actuator of the lateral load system.

2.5. Instrumentation.

The instrumentation placed in the specimens is shown in Figure 7 and Figure 8. In the Ni-Ti SMA bars, 16 strain gauges were placed in four sections located in the critical zone of the column with four thermocouples in a section close to the embedment between the column and the foundation (Figure 7). However, all gauges on all specimens failed shortly after testing began. The cause was a problem with the data acquisition system. In addition, 27 linear variable differential transformers (LVDTs) were placed. Devices 1-11 recorded the specimen's lateral displacement (Figure 7). The rotation of the foundation was obtained from the records of devices 10 and 11. Devices 11-23 (Figure 8.a) were designed to indirectly record the average bending curvature at six sections from the column foundation interface. In the specimens with a protruding bar connection type, four LVDTs were placed (devices 24-27) to record the possible joint displacements (Figure 8.b). Finally, a synchronised recording system was used where each photogram was assigned to the corresponding applied load (Figure 6.a).

2.6. Test procedure.

All the specimens were tested 28 days after manufacturing the column (Table 1). The test room temperature was set at 18-20°C. First of all, a horizontal load corresponding to the relative normal force was applied and remained constant throughout the test. The lateral load was then applied with displacement control at a constant velocity of 0.2±0.05 mm/min.

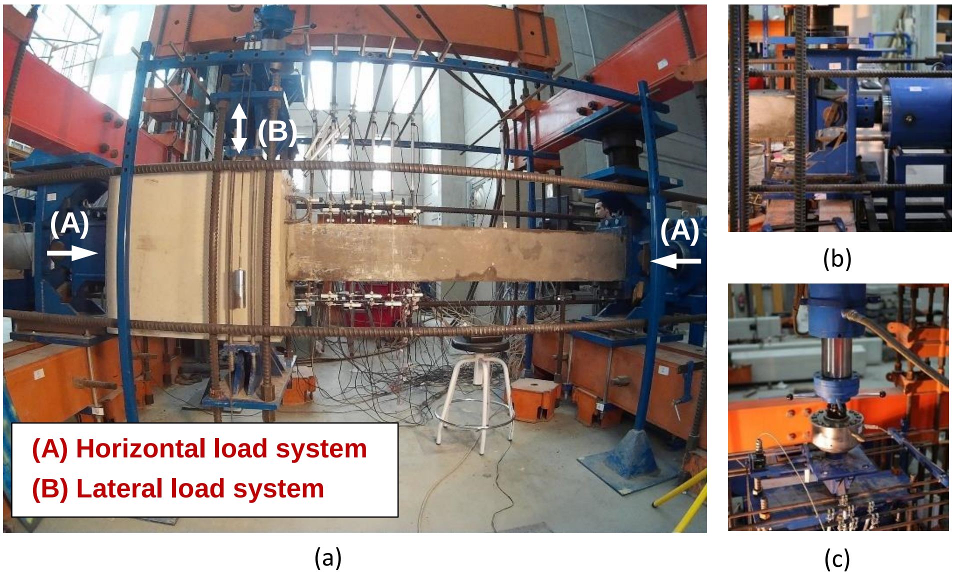

Figure 6: The outer test configuration: (a) global set-up; (b) hydraulic actuator that applies the axial load; (c) hydraulic actuator that applies the lateral load.

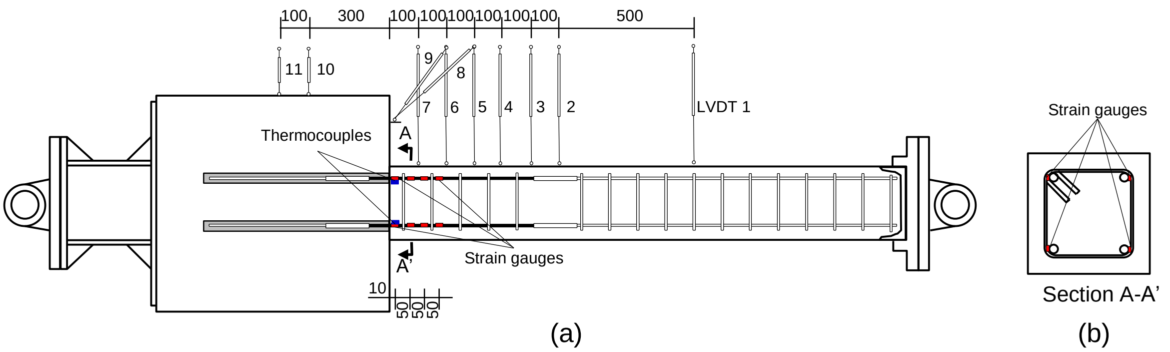

Figure 7: Lateral displacement measurements and location of strain gauges and thermocouples (unit: mm): (a) frontal view; (b) section A-A'.

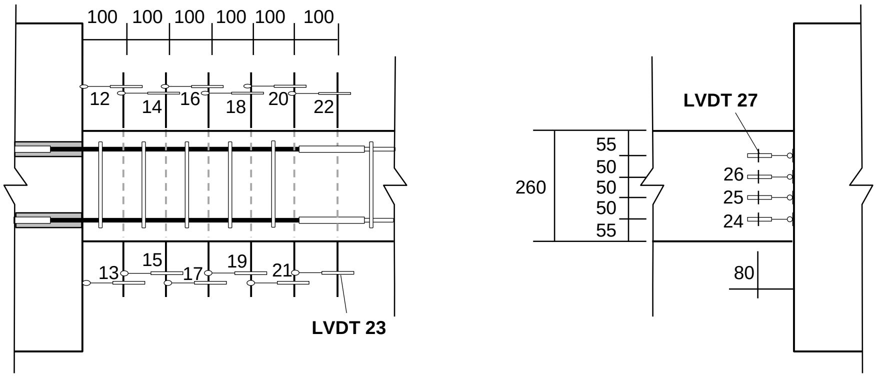

(a) (b)

Figure 8: Horizontal displacement measurements (unit: mm): (a) LVDTs in the connection; (b) LVDTs in the joint of the specimens with a protruding bar connection type.

The test sequence of the displacement-controlled cycles is expressed in terms of drift ratio (Δ/L_s). For each drift ratio, three complete cycles were applied (Figure 9), as defined in ACI 374.1[61], FEMA-356 [62] and P-750-FEMA [63]. The drift ratio Δ/L_s is obtained by dividing the Δ displacement at the end of the column in each direction and the length of column L_s. The effect of an earthquake was simulated by applying this quasi-static lateral load with incremental displacement cycles. Figure 10 shows how the Δ displacement at the end of the column was calculated.

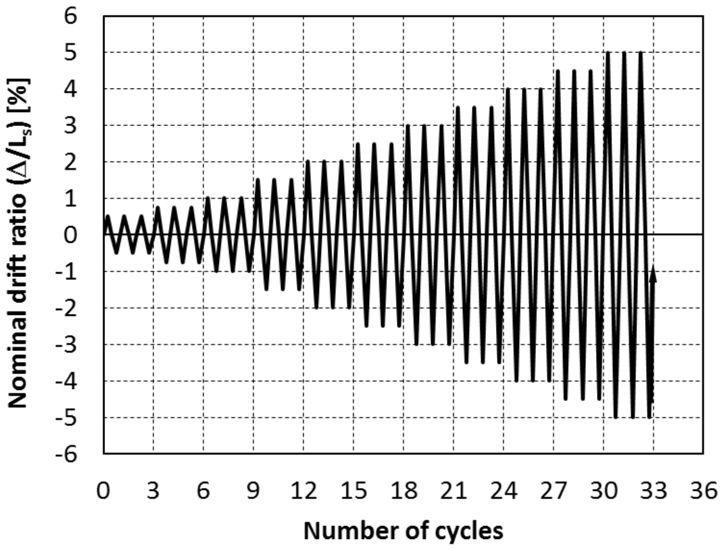

Figure 9: Cyclic loading protocol.

3. Test observations.

Figure 11 shows the specimens' behaviour for a drift ratio (Δ/L_s) of approximately 5%, where the shear force (V) is practically zero and there is at least a 20% lateral load (V') loss (Figure 10). The following general observations were made:

1. Distributed cracking was observed in the area of the connection between the column and the foundation. The connection was painted with a water-repellent varnish to detect the cracking pattern. When the test finished, it was soaked with water to observe the cracking pattern (Figure 11).

2. The joint between the column and the foundation opened in the specimens with a protruding bar connection type (Z1-PBV02 and Z2-PBV02). In this case, the connection showed rocking behaviour by minimising the damage between the foundation and the column. The tensile strength of the epoxy resin placed between the column and the foundation was insufficient, and caused the joint between the column and the foundation to open (gap opening) (Figure 11.a and Figure 11.b). This behaviour was due to: the high content of steel fibres in UHPC, which allows it to achieve a high compressive strain without undergoing concrete crushing or concrete cover spalling in the joint between the column and the foundation; the high content of steel fibres in UHPC, which prevents buckling in the Ni-Ti SMA compressed bars despite the deformation modulus being approximately 3-fold lower than in conventional steel bars [28]; the fact that the Ni-Ti SMA bars can high significant tensile and compressive strains; the fact that the bond strength between the polished Ni-Ti SMA bar and UHPC concrete reduced by more than 70%, or even more due to cyclic loads compared to the corrugated bars [64,65]. This last fact led the strain to distribute along the bar length between couplers, which prevent the strains of the bar from concentrating at the joint, which would lead to brittle tensile failure. However, the loss of bond causes a large development length of SMA rebars and energy dissipation is reduced. The minimisation of damage in UHPC and the superelastic behaviour of the Ni-Ti SMA bars allowed the residual deformations at the joint, and therefore at the column, to be minimised.

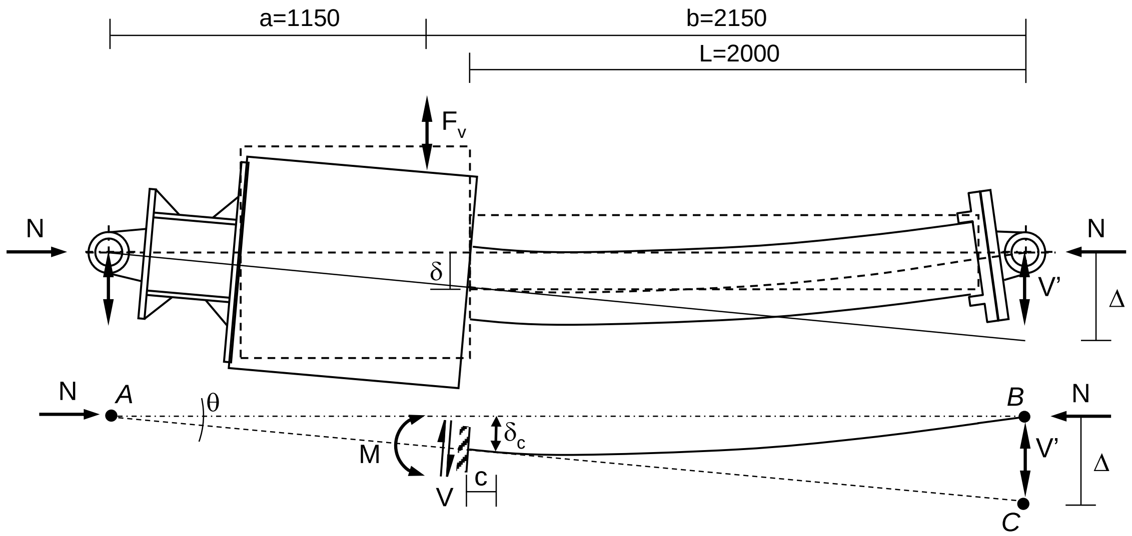

$$V' = F_v \frac{a}{a+b}; \quad \Delta = \delta \frac{a+b}{L}; \quad \theta = \Delta/(a+b); \quad V = V' cos\theta - N sin\theta$$

$$M(x = c) = N \cdot \delta_c + V' \cdot (L - c)$$

Figure 10: Specimen idealisation.

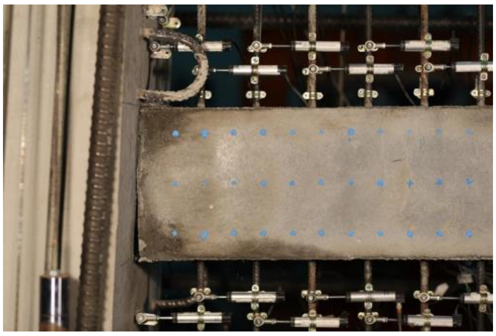

(a) Z1-PBV02 (Δ/L_s=5%)

(b) Z2-PBV02 (Δ/L_s=5%)

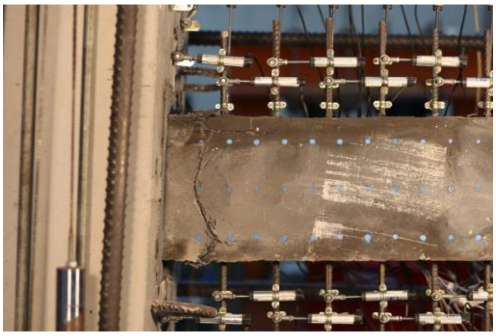

(c) Z3-SPV02 (Δ/L_s=4%)

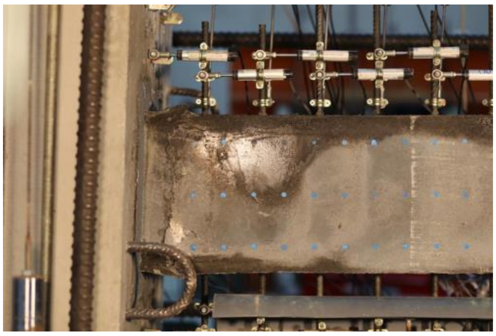

(d) Z4-SPV02 (Δ/L_s=4%)

Figure 11: specimen behaviour at ultimate state: (a) specimen Z1-PBV02; (b) specimen Z2-PBV02; (c) specimen Z3-SPV2; (d) specimen Z4-SPV02.

3. In the specimens with a SP connection type (Z3-SPV02 and Z4-SPV02), a single main crack appeared and was slightly displaced from the interface between the column and the foundation

(Figure 11.c and d). It should be noted that the crack in specimen Z3-SPV02 had the appearance of a joint (Figure 11.c). Once the main crack had formed, the column displayed a rocking behaviour in that critical section. In this case, this movement produced greater concrete degradation (both in tension and compression) compared to the PB connection. The superelastic behaviour of the Ni-Ti SMA bars, together with a slight damage of UHPC, allowed the minimisation of the residual deformations in this section, and therefore in the column.

4. The critical section in the specimens with a PB connection type (Z1-PBV02 and Z2-PBV02) was located at the joint of the column with the foundation; that is, $c = 0$ (Figure 10). In the specimens with a SP connection type, the critical section moved from the joint between the column and the foundation (stub effect) despite being subjected to the maximum bending moment. This phenomenon can be explained by the confinement effect caused by the foundation in the nearby sections of the column (Khoury and Sheikh [66] and Paultre et al. [67]). Consequently, the critical section was displaced over a distance $c = 70\,mm$ from the joint between the column and the foundation in specimens Z3-SPV02 and Z4-SPV02 (Figure 10).

5. No buckling of the Ni-Ti SMA bars in compression was observed.

6. In all the specimens, the concrete cover degraded but did not spall (Figure 11), although it was more significant in the columns with a SP connection type (Z3-SPV02 and Z4-SPV02).

7. No cracking, failure or sliding of the grout of the SP specimens was observed.

4. Results and Discussion.

4.1. Test results.

As Liu (2013) [68] stated, when lateral deflection Δ and applied axial load N are large, the difference between the lateral shear force (V) and the applied lateral load (V') can be significant (Figure 10). Figure 12 provide an example of the comparison between the V-Drift ratio and V'-Drift ratio for specimen Z1-PBV02 with an applied axial load N equalling 1627.81 kN. In this figure, a very large difference between V and V' is observed. It should be noted, for this example, that the compressive force on the AC axis of the column was 1629.22 kN for the maximum drift ratio (Δ/L_s) recorded during the test (6.29%). This value is similar to the applied axial load along the original axis AB, equalling 1,627.81 kN (Figure 10). Consequently, specimens can be considered subjected to a constant uniform axial force that equalled the applied axial load throughout the cyclic lateral load test. Sectional behaviour was represented by the moment-curvature relation at the critical cross-section. The critical section in the specimens with a PB connection type was located at the joint between the column and the foundation, where the moment was longest. However in the specimens with a SP connection type, the critical section was displaced by a distance c from the foundation, as indicated by the most damaged region (Figure 10). This moment was obtained as the sum of a primary moment caused by the applied lateral cyclic load (V') and a secondary moment caused by the applied axial load N.

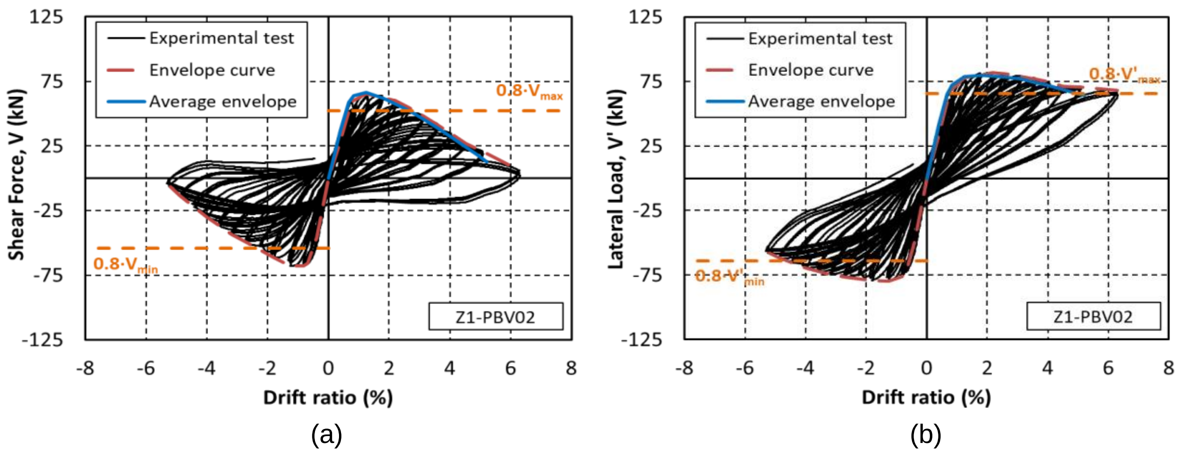

Figure 12: Comparison between shear force V and lateral load V' of Z1-PBV02: (a) V-Drift ratio curve (b) V'-Drift ratio curve.

Figure 13 shows the experimental results for the shear force V-Drift ratio. In these curves, the experimental response V-Drift ratio for the load cycles until the specimen had a 20% lateral load (V') loss, which corresponded to a practically null shear force (V), is represented by a solid black line. For the other cycles, it is represented by a solid grey line. In addition, the limit value corresponding to 20% capacity loss ($0.8 \cdot V_{max}$ or $0.8 \cdot V_{min}$) is marked in the graphs. Figure 14 provides the experimental results of the total bending moment-average curvature at the critical section. The limit value corresponding to 20% capacity loss ($0.8 \cdot M_{max}$ or $0.8 \cdot M_{min}$) is marked in these graphs. The average curvature was obtained from the readings of LVDTs 12 and 13 (Figure 8).

In all the specimens, the maximum shear force was reached, and a descending branch was observed (Figure 13). However, it was only on the moment-curvature curve of specimens Z3-SPV2 and Z4-SPV02 (Figure 14.c and d) that the maximum strength value of the critical section was reached, and a descending branch was observed. In the other specimens (Figure 14.a and b), after exceeding the plastic moment, the moment-curvature curve trend showed that the maximum experimental value of the bending moment was similar to the maximum moment resistance of the critical section.

In the case of SP specimens, the critical section reached the peak moment when the specimen supported the peak lateral load. This indicates that the failure mode of specimen was the failure of the materials, specifically the concrete. In the case of PB specimens, the bearing moment of the section remains constant (plastic moment) after the specimen reaches the maximum lateral load. This indicates that the failure is caused by instability. That is, the P-delta effect caused the second order moments to be large in the critical section, to the point that they exceed the plastic moment that the section withstood and, consequently, the cyclic lateral load necessarily decreased.

Lastly, Table 4 summarises the main experimental results.

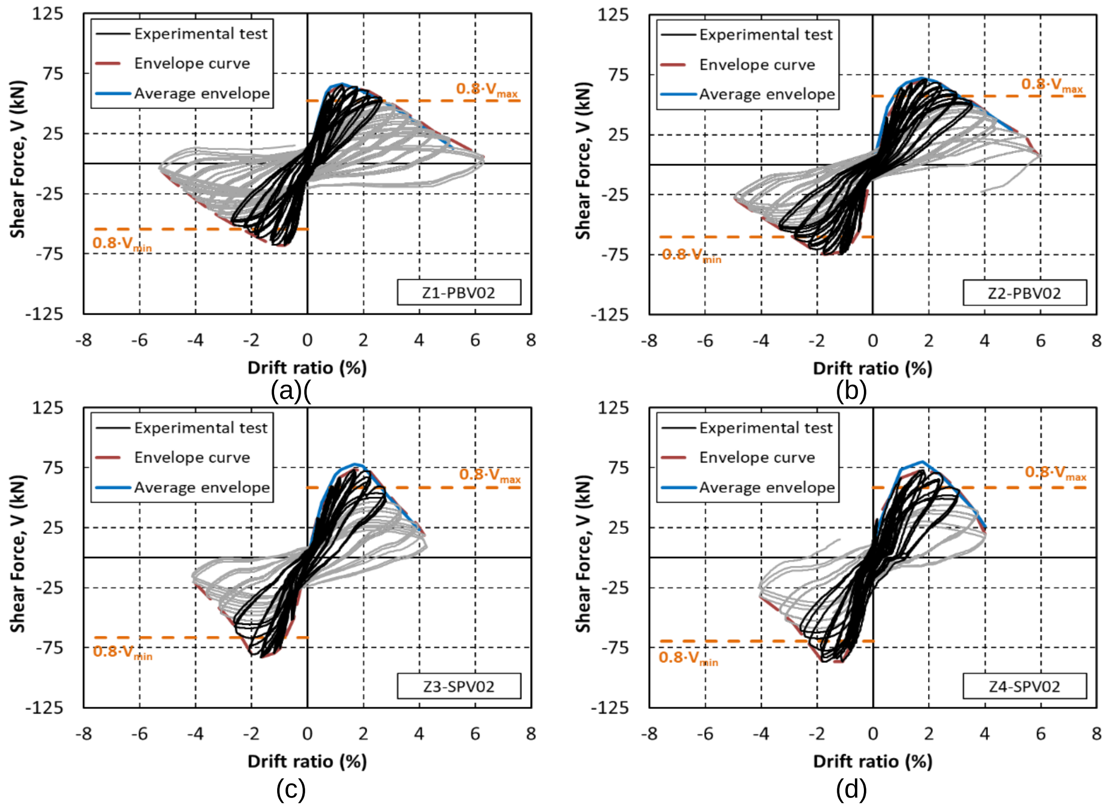

Figure 13: Experimental shear force – drift ratio curves: (a) specimen Z1-PBV02; (b) specimen Z2-PBV02; (c) specimen Z3-SPV2; (d) specimen Z4-SPV02.

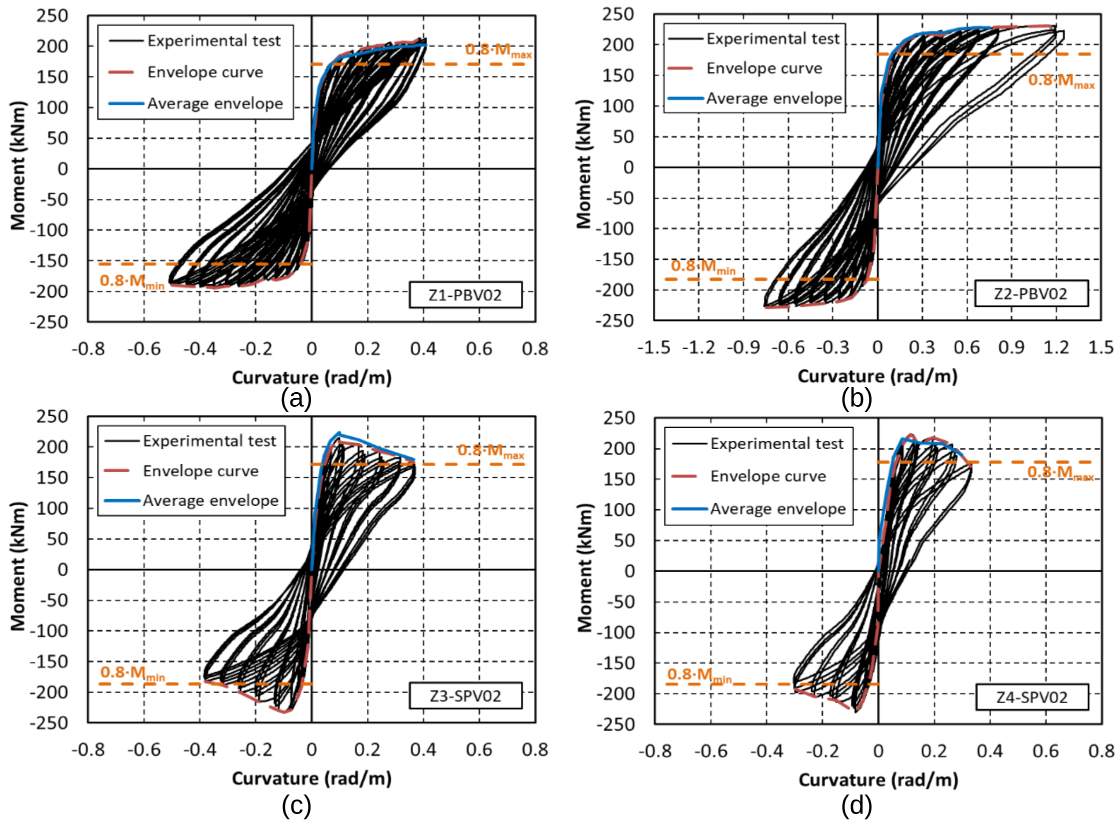

Figure 14: Experimental moment - curvature curves: (a) specimen Z1-PBV02; (b) specimen Z2-PBV02; (c) specimen Z3-SPV2; (d) specimen Z4-SPV02.

Table 4: Summary of the experimental results.

Id	Specimen	V_{max} (kN)	$\frac{V_{max}}{b \cdot h \cdot f_c}$	Δ_{yI} (mm)	Δ_u (mm)	$\mu_{\Delta u}$	M_{max} (kNm)	$\frac{M_{max}}{b \cdot h^2 \cdot f_c}$	φ_{yI} (10^{-3} rad/m)	φ_u (10^{-3} rad/m)	$\mu_{\varphi u}$	E_{sum} (kNm)	E_N	K_0 (kN/m)
1	Z1-PBV02	66.49	0.0082	14.92	51.49	3.45	203.08	0.096	58.35	407.57	6.98	27.91	14.31	4515.25
2	Z2-PBV02	72.19	0.0084	18.08	60.98	3.37	228.44	0.103	93.41	747.90	8.01	26.98	10.14	4537.94
3	Z3-SPV02	78.03	0.0095	20.36	49.64	2.44	223.55	0.104	47.14	364.36	7.73	25.82	10.91	4594.97
4	Z4-SPV02	79.83	0.0097	20.08	52.36	2.61	215.74	0.101	56.94	299.00	5.25	23.28	11.42	4208.88

4.2. Strength capacity.

Table 4 shows the relative maximum shear force $V_{max}/(f_c \cdot b \cdot h)$ and the relative maximum bending moment in the critical section $M_{max}/(f_c \cdot b \cdot h^2)$ reached in each test, where f_c is the compressive strength of the precast column UHPC. In both cases, the effects of own weight (for calculating the bending moment and shear force) were considered. Second-order effects were also contemplated for the bending moment calculation. We see that the relative maximum shear force was similar in the two specimens with the same connection type. Furthermore, and as expected, strength capacity $V_{max}/(f_c \cdot b \cdot h)$ was greater in the specimens with a SP connection type (Z3-SPV02 and Z4-SPV02) as the joint between the column and the foundation in the PB connection type (Z1-PBV02 and Z2-PBV02) had no flexural tensile strength capacity, while continuity in the column was noted in specimens Z3-SPV02 and Z4-SPV02. It is noteworthy that the value of the maximum moment reached $M_{max}/(f_c \cdot b \cdot h^2)$ in the four specimens was similar because the flexural tensile strength capacity in the critical section was non-existent in the joint between the column and the foundation in specimens Z1-PBV02 and Z2-PBV02, or was lower in specimens Z3-SPV02 and Z4-SPV02 as the gap opening (crack opening) in the critical section was significant.

4.3. Deformation capacity.

Figure 15 shows the idealisation of the actual envelope diagram [69,70] shear force-tip displacement $(V - \Delta)$ or moment-curvature $(M - \varphi)$ in a bilinear diagram, made up of an elastic branch and a decreasing inelastic branch. By means of the bilinear diagram, it is possible to calculate the ultimate displacement ductility $\mu_{\Delta u} = \Delta_u/\Delta_{yI}$, where Δ_u is the ultimate displacement of the column corresponding to 0.80 of the maximum load on the descending branch, and Δ_{yI} is the effective elastic displacement. The ultimate curvature ductility $\mu_{\varphi u} = \varphi_u/\varphi_{yI}$, where φ_u is the ultimate curvature of the section corresponding to 0.80 of the maximum moment on the descending branch, and φ_{yI} is the effective elastic curvature.

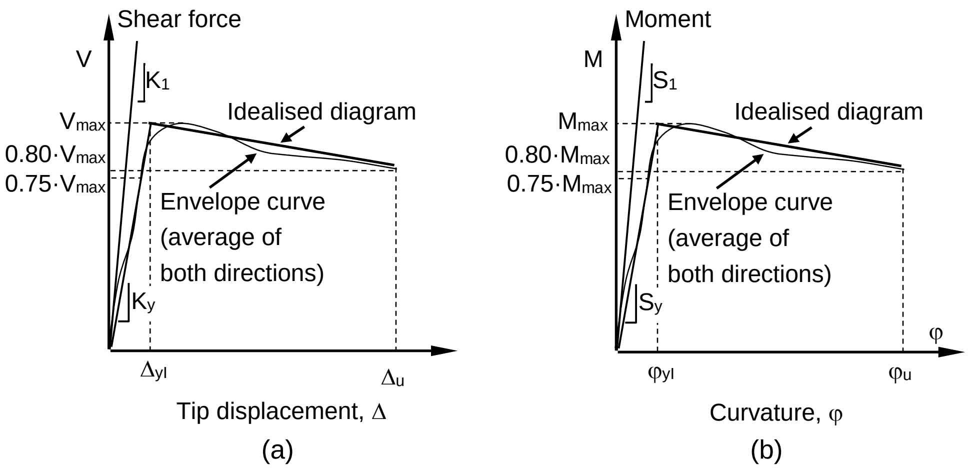

Figure 15: Ideal curve definitions.

Table 4 shows the ductility results of each specimen. Specimens Z3-SPV02 and Z4-SPV02 developed displacement ductility $\mu_{\Delta u}$ came close to 3 (high ductility according to NCSE-02 [5]). Specimens Z1-PBV02 and Z2-PBV02 had displacement ductility between high ductility $(\mu_{\Delta u} = 3)$

and very high ductility ($\mu_{\Delta u} = 4$). All ductilities were high because of the use of advanced materials (UHPC and Ni-Ti SMA). UHPC allowed us to achieve significant compressive strains that delayed concrete cover spalling, and the buckling of compressed reinforcement buckling and concrete. Ni-Ti SMA bars can reach significant tensile and compressive strains because its intrinsic ductile behaviour. Furthermore, the required strain of the gap opening was distributed along the NiTi-SMA bar between couplers because the lack of bond Ni-Ti bars – concrete due to the polished surface of these bars.

PB connection specimens underwent more displacement ductility than SP connection specimens because critical section was located at the column-foundation interface in PB connection specimens, which allowed a moment-rotation behaviour of the connection without causing significant damage or strength degradation. However, a crack opened in the critical zone in SP connection specimens at 70 mm from the column-foundation joint. Degradation of the flexural tensile strength in the post-peak load zone occurred, which resulted in greater strength capacity loss for the same displacement increase in these specimens than in the specimens with a PB connection.

Regarding curvature ductility $\mu_{\varphi u}$, the mean value of PB connection specimens was 7.50 and was 6.49 for the SP specimens. Nevertheless, as it was not possible to observe a descending branch on the moment-curvature curve in specimens Z1-PBV02 and Z2-PBV02 (Figure 14), the curvature ductility shown in Table 4 is a lower bound in specimens Z1-PBV02 and Z2-PBV02. The reason why PB connection specimens developed more curvature ductility is the same exposed when analysing displacement ductility. In all specimens, a higher curvature ductility value than that expected was obtained if the conservative expression that related both ductilities ($\mu_{\varphi u} = 2\mu_{\Delta u} - 1$) from EC-8 [1] was used.

Specimens with the same geometry (same cross section, slenderness and longitudinal reinforcement ratio) made of plain conventional concrete with nominal compressive strength of 30 MPa and with SP and PB type connection were tested by Romero-García et al. [1]. The differences with the specimens of this research were: the separations of stirrups were 5 cm instead of 10 cm, the longitudinal bars in the critical section were of steel instead of SMA, and the concrete type. The relative axial loads studied were 0.1, 0.3 and 0.45. The displacement ductilities were: 3.09 for PB specimen and 2.94 for SP specimen, both for a relative axial load of 0.3. In case of relative axial load of 0.1, ductilities for PB and SP specimen were 4.28 and 3.75, respectively. All the results are depicted in Table 5.

As is known, if the concrete compressive strength increases, the ductility decreases if the rest of the parameters remain constant. To avoid this, either more transverse reinforcement ratio is provided, or steel fibres are added into the concrete. In our case, UHPC has 2% of steel fibres by volume. In this way and according to Table 5, the ductility of the UHPC-SMA specimens (with relative axial load of 0.2) is between the ductility of the plain normal strength concrete specimens tested by Romero-García et al. [1] for ductilities 0.1 and 0.3. As a consequence, the expected ductility of both specimen types (plain normal strength concrete specimens and UHPC-SMA specimens) for the same relative axial load would be similar, even when transverse reinforcement ratio was lesser in UHPC-SMA specimens. However, the load strength was approximately three time higher using the new materials of these research and the residual drift ratios were smaller. The degradation of the materials was also lesser.

As a synthesis, the specimens showed in this research increased the load strength capacity, decreased residual drift ratios and materials degraded lesser than reference specimens by keeping the ductility.

Table 5: Comparison between results of Romero-García et al. [1] specimens and specimens of this research.

Specimen	f_c (MPa)	Connection type	Relative axial load	V_{max} (kN)	$\mu_{\Delta u}$
Z1-PBV02	70.35	PB	0.2	66.49	3.45
Z2-PBV02	48.51	PB	0.2	72.19	3.37
Z3-SPV02	67.09	SP	0.2	78.03	2.44
Z4-SPV02	61.03	SP	0.2	79.83	2.61
SP-L08-N1-S1-F00 [1]	28.40	SP	0.1	27.86	3.75
PB-L08-N1-S1-F00 [1]	30.30	PB	0.1	26.69	4.28
RP-L08-N1-S1-F00[1]	26.90	RP	0.1	26.14	3.59
BS-L08-N1-S1-F00 [1]	29.60	BS	0.1	24.12	4.11
SP-L08-N3-S1-F00 [1]	32.80	SP	0.3	36.35	2.94
PB-L08-N3-S1-F00 [1]	34.48	PB	0.3	36.11	3.09
RP-L08-N3-S1-F00 [1]	34.70	RP	0.3	30.11	4.32
BS-L08-N3-S1-F00 [1]	34.10	BS	0.3	28.63	3.01

4.4. Energy dissipation.

The energy dissipation corresponding to each j-cycle of the ith drift ratio hysteretic loop is defined as (Figure 16):

$$E_i^j = \oint_A^B V d\Delta \quad (1)$$

The total dissipated energy during the test can be expressed as:

$$E_{sum} = \sum_i^{m_1} \sum_j^{m_2} E_i^j \quad (2)$$

where E_{sum} is cumulate dissipated energy; m_1 is the number of the drift ratio until the specimen takes 20% shear force loss, which approximately corresponds to a target drift of 3%; m_2 is the number of cycles for each drift ratio. To compare the dissipated energy between elements, normalised dissipated energy E_N is calculated as [71]:

$$E_N = \sum_i^{m_1} \sum_j^{m_2} [E_i^j / (V_i^j \Delta_i^j)] \quad (3)$$

$$\Delta_i^j = (|\Delta_i^{j+}| + |\Delta_i^{j-}|)/2, \; V_i^j = (|V_i^{j+}| + |V_i^{j-}|)/2 \quad (4)$$

where Δ_i^{j+} and Δ_i^{j-} are the maximum displacements corresponding to the jth cycle in the ith drift ratio in the pull and the push direction, respectively; V_i^{j+} and V_i^{j-} are the shear forces corresponding to Δ_i^{j+} and Δ_i^{j-}, respectively.

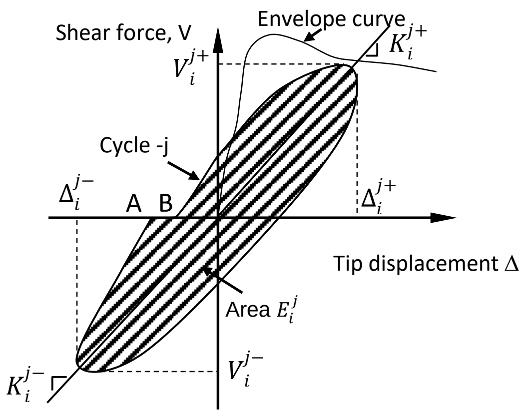

Figure 16: Energy dissipation.

Table 4 offers the results of the total dissipated energy and normalised energy of all the specimens. Similar energy was dissipated in the two connection types.

4.5. Stiffness degradation.

The column stiffness (K_i) in the i[th] drift ratio is defined as [71]:

$$K_i = \sum_{j=1}^{m_2} V_i^j / \sum_{j=1}^{m_2} \Delta_i^j \quad (5)$$

where K_i is the mean secant stiffness at the i[th] drift ratio level; Δ_i^j and V_i^j are defined in Equation (4). To compare the results, normalised column stiffness η_{K_i} is calculated by dividing by the stiffness in a drift ratio of 0.5% (K_0) as columns maintain an elastic behaviour for this drift ratio.

$$\eta_{K_i} = K_i / K_0 \quad (6)$$

Table 4 shows the results of K_0. The mean stiffness K_0 value equalled 4464.26 kN/m, which is similar to the mean values for each connection type (4526.6 kN/m for the PB connection and 4401.93 kN/m for the SP connection type). Consequently, there were no significant differences in the mean values between both connection types. Figure 17 depicts normalised column stiffness η_{K_i} of all the specimens according to the drift ratio. In general, until the maximum shear force V_{max} was reached, specimens with PB connection had lower relative stiffness. Thus, in all the specimens, and for the same applied axial load level, as the drift ratio rose, the bending moment in the critical section increased and, consequently, the depth of the neutral axis reduced, which required a greater curvature. This greater curvature in specimens with PB connection meant a more marked reduction in normalised stiffness η_{K_i} because, there was no flexural tensile strength in the critical section of these specimens located at the joint between the column and the foundation, unlike in specimens with SP connection, where the steel fibres in the critical section conferred residual flexural tensile stiffness. However, this trend was reversed for a higher drift ratio than the drift ratio in which V_{max} was reached because degradation occurred in the critical section in in specimens with SP connection in both compression and tension, which involved greater stiffness loss in the descending branch of the shear force-drift ratio curve compared to that observed in specimens with PB connection.

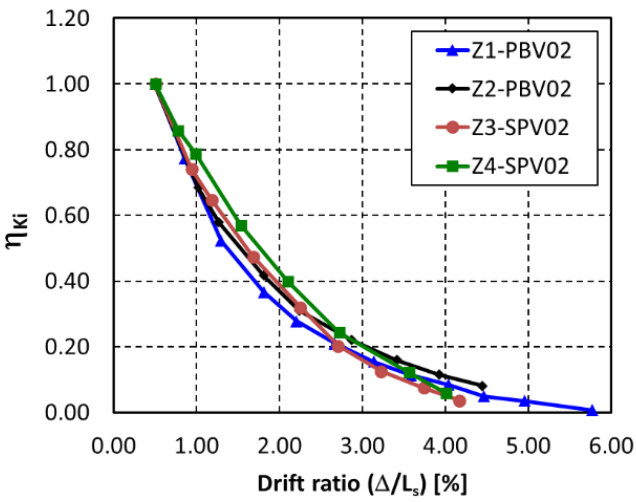

Figure 17: Stiffness degradation of the specimens.

4.6. Residual drift ratio.

The mean residual drift ratio ($D_{r,i}$) of the column in the ith drift ratio is defined as:

$$D_{r,i} = \left(\left|D^{+}_{r,i}\right| + \left|D^{-}_{r,i}\right|\right)/2 \tag{7}$$

$$D^{+}_{r,i} = \sum_{j=1}^{m_2} D^{+}_{r,ij}/m_2\,;\; D^{-}_{r,i} = \sum_{j=1}^{m_2} D^{-}_{r,ij}/m_2 \tag{8}$$

where $D^{+}_{r,i}$ and $D^{-}_{r,i}$ are the average value of the residual drift ratio in the ith drift ratio in the pull and the push direction, respectively; $D^{+}_{r,ij}$ and $D^{-}_{r,i}$ are the residual drift ratio of the jth cycle at the ith drift ratio in the pull and the push direction, respectively; m_2 is the number of cycles of each ith drift ratio. The mean residual drift ratio was analysed until the specimen displayed 20% shear force loss, which corresponds approximately to a 3% target drift.

Figure 18 shows the mean residual drift ratio of the column in the ith drift ratio for all the specimens up to a drift ratio of between 3% and 4%. As we can see, the mean residual drift ratio values went below 0.5% for drift ratios below 2.5%. Up to this drift ratio, no significant differences appeared between the connection types of the column with the foundation. The lowest mean residual drift ratio was related to the lowest degradation of the critical section on the joint in the specimens with a PB connection type compared to the damage noted in the critical section in the specimens with a SP connection type. The reduced residual deformations in the column resulted in the structure undergoing self-centring capacity. This behaviour was because the damage in UHPC was slight and was due to the superelasticity of the Ni-Ti SMA bars.

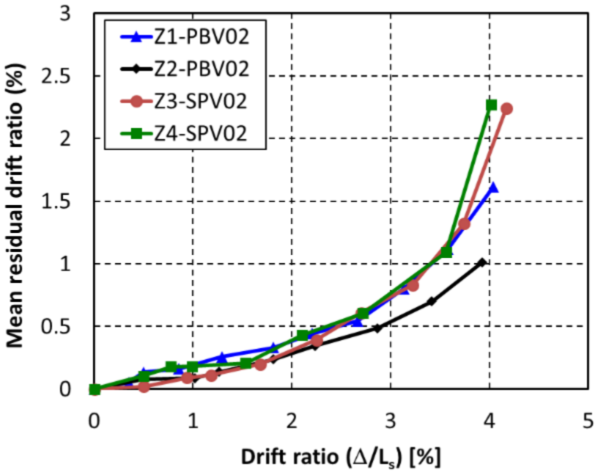

Figure 18: Residual drift ratio.

4.7. Gap opening displacement in the joint between the column and foundation.

In the specimens with a PB connection between the column and the foundation, four LVDTs (devices 24-27) were placed to record the possible displacements of the joint (Figure 8.b).

Figure *19* provides as an example of the displacements of specimen Z2-PBV02 in the position of the LVDTs for the different drift ratios (Δ/L_s). In this figure, a linear interpolation for each drift ratio was made, which gave sufficient approximation ($R^2 \approx 1$) to represent the strain plane. Rocking movement of the joint is observed on the pull and push direction of lateral load, with major gap opening of > 6 mm in some cases. As expected, because the target drift ratio increased, the compressive zone depth decreased. The changes in the neutral axis depth through this gap opening and the development of non-linear-inelastic compressive concrete behaviour brought about the moment-rotation behaviour of the connection without causing any significant damage or strength degradation. This was caused because of: (1) the bond loss of the Ni-Ti SMA bars that distributed the strain along the entire rebar; (2) the very ductile behaviour of these bars; (3) the use of UHPC with a high-fibre content.

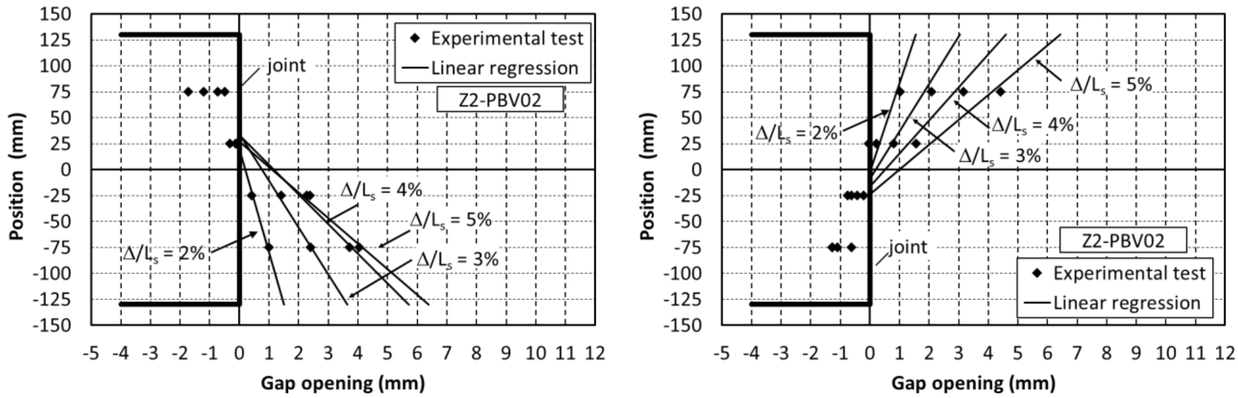

(a) (b)

Figure 19: Gap opening displacement in the joint between the column and the foundation (specimen Z2-PBV02).

If the lateral load was zero, the joint remained compressed due to the recovery of the Ni-Ti bars (superelasticity), and also because the concrete did not show any significant degradation in the joint. The high steel fibres content in UHPC allowed a significant compressive strain to be achieved

5. Summary and Conclusions.

The experimental behaviour of the precast column-to-foundation connection under lateral reversed cyclic loading and constant axial load was studied. The column was manufactured with ultrahigh-performance concrete (UHPC) with high steel fibre content (volumetric steel/fibre ratio of 1.9%). The steel bars in the connection were replaced with Ni-Ti SMA bars with superelasticity. These Ni-Ti SMA bars crossed the interface between the column and the foundation. Two types of connection between the column and the foundation were analysed: protruding bars (PB) and smooth pocket (SP). All the specimens were subjected to the same constant level of relative axial load ($\nu = 0.20$). Two specimens were tested for each connection type. All the results of the four experimental tests are presented.

From the experimental results, it was concluded that:

– The response of the PB connection showed rocking behaviour where the rotation through the gap opening at the joint between the column and foundation concentrated. The neutral axis depth was reduced with gap opening and, therefore, the strains in the section increased in both compression in UHPC and the Ni-Ti SMA bars and in tension in the Ni-Ti SMA bars. The use of advanced materials (UHPC and Ni-Ti SMA) allowed these strains to develop without causing significant damage. Thus the use of UHPC with high fibre content allowed us to achieve significant compressive strains that delayed concrete cover spalling, and compressed reinforcement buckling. The Ni-Ti SMA bars can achieve significant tensile and compressive strains with very ductile behaviour. Furthermore, the polished surface of these bars allowed the bond with concrete to reduce, and the required strain of the gap opening was distributed along the NiTi-SMA bar between couplers. Little concrete damage and the superelastic Ni-Ti SMA bars mean that the residual deformations in the specimen were minimum. The mean residual drift ratio was under 0.5% for drift ratios below 2.5%.

– In the specimens with SP connection type, a single main crack appeared, and was slightly displaced from the interface between the column and the foundation. The specimen showed rocking behaviour in this critical section. This behaviour was possibly due to: adequate UHPC behaviour in compression; the fact that the Ni-Ti SMA bars can achieve significant tensile and compressive strains; the bond reduction between the Ni-Ti SMA bars and UHPC. The damage in the critical section was greater than in the PB connection type, mainly due to the degradation of concrete in tension. However, residual deformations were minimal due to the low UHPC damage and the superelasticity of the Ni-Ti SMA bars. The mean residual drift ratio was lower than 0.5% for drift ratios below 2.5%.

– In the specimens with the SP connection type, strength capacity $V_{max}/(f_c \cdot b \cdot h)$ was greater given the continuity of the column with the foundation, and because the column-to-foundation joint had no flexural tensile strength in the PB connection type. However, the PB connection showed greater displacement ductility $\mu_{\Delta u}$ because the existence of the joint allowed a moment-rotation behaviour of the connection without causing significant damage or strength degradation. Both connection types dissipated energy E_N and initial stiffness K_0 that were similar. No significant differences were observed for the stiffness degradation with the drift ratio.

The above conclusions have been drawn for a limited number of specimens. A greater number of tests would be necessary to obtain relevant conclusions.

The entire specimen was manufactured with UHPC in this research. However, this design should be optimized in the future, so that UHPC is only used in a length of the column close to the foundation and the rest is made of lower performance concrete. This study has already been carried out for in-situ column-beam connections by Pereiro-Barceló el al. [6] and they found that the use of UHPC was only necessary in a small column length.

6. Acknowledgements.

This paper forms part of a research line carried out at the University Institute of Concrete Science and Technology (ICITECH) of the Universitat Politècnica de València. The authors wish to thank to the Spanish Ministry of Science and Innovation for the support it provided through Projects BIA2012-32645 and RTI2018-099091-B-C21-AR, and grant BES-2016-078010, to the European Union for the financial support with FEDER funds and to the Spanish Ministry of Education, Culture and Sport for grant FPU12/01451.

References

[1] European Commitee for Standardization. Eurocode 8 - Design of structures for earthquake resistance - Part 1: General rules, seismic actions and rules for buildings. 2004. https://doi.org/[Authority: The European Union per Regulation 305/2011, Directive 98/34/EC, Directive 2004/18/EC].

[2] FEMA. NEHRP Recommended Seismic Provisions for New Buildings and Other Structures FEMA P-750 2009.

[3] ACI committee 318. 318-19: Building Code Requirements for Structural Concrete and Commentary. 2019.

[4] Fomento EM de, Hormigón ECP del. EHE-08 : Instrucción de hormigón estructural : con comentarios de los miembros de la Comisión Permanente del Hormigón. Ministerio de Fomento, Secretaría General Técnica; 2010.

[5] NCSE-02. Norma de Construcción Sismorresistente: Parte general y edificación (NCSE-02). J Chem Inf Model 2013;53:1689–99. https://doi.org/10.1017/CBO9781107415324.004.

[6] Hsu LS, Hsu CTT. Stress-strain behavior of steel-fiber high-strength concrete under compression. ACI Struct J 1994;91:448–57. https://doi.org/10.14359/4152.

[7] Foster SJ. On behavior of high-strength concrete columns: Cover spalling, steel fibers, and ductility. ACI Struct J 2001;98:583–9. https://doi.org/10.14359/10301.

[8] Aoude H, Cook WD, Mitchell D. Behavior of columns constructed with fibers and self-consolidating concrete. ACI Struct J 2009;106:349–57. https://doi.org/10.14359/56499.

[9] Campione G, Fossetti M, Papia M. Behavior of fiber-reinforced concrete columns under axially and eccentrically compressive loads. ACI Struct J 2010;107:272–81. https://doi.org/10.14359/51663692.

[10] Paultre P, Eid R, Langlois Y, Ĺvesque Y. Behavior of steel fiber-reinforced high-strength concrete columns under uniaxial compression. J Struct Eng 2010;136:1225–35. https://doi.org/10.1061/(ASCE)ST.1943-541X.0000211.

[11] Caballero-Morrison KE, Bonet JL, Navarro-Gregori J, Martí-Vargas JR. Behaviour of steel-fibre-reinforced normal-strength concrete slender columns under cyclic loading. Eng Struct 2012;39:162–75. https://doi.org/10.1016/j.engstruct.2012.02.003.

[12] Romero-García A, Bonet JL, Martí-Vargas JR, Navarro-Gregori J. Behaviour of precast columns to-foundation connections under cyclic loading. 15th World Conf Eatrhquake Eng 2012:24–8.

[13] Markovic I. High-Performance Hybrid-Fibre Concrete: Development and Utilisation. Delft: DUP

Science; 2006.
[14] ASTM C1856 / C1856M - 17: Standard Practice for Fabricating and Testing Specimens of Ultra-High Performance Concrete n.d.
[15] Perry VH (Vic. What Really Is Ultra-High Performance Concrete - Towards a Global Definition. 2018.
[16] Walraven JC. High performance fiber reinforced concrete: Progress in knowledge and design codes. Mater Struct Constr 2009;42:1247–60. https://doi.org/10.1617/s11527-009-9538-3.
[17] Brühwiler E, Denarié E, Habel K. Ultra-high performance fibre reinforced concrete for advanced rehabilitation of bridges. vol. 2. 2005.
[18] Guerrini GL. Applications of High-Performance Fiber-Reinforced Cement-Based Composites. Appl Compos Mater 2000;7:195–207.
[19] Walraven J. High performance concrete: A material with a large potential. J Adv Concr Technol 2009;7:145–56. https://doi.org/10.3151/jact.7.145.
[20] Castro C. Análisis experimental de soportes de hormigón de altas prestaciones sometidos a compresión y carga lateral cíclica. Universitat Politècnica de València, 2016.
[21] Pansuk W, Nguyen TN, Sato Y, Den Uijl JA, Walraven JC. Shear capacity of high performance fiber reinforced concrete I-beams. Constr Build Mater 2017;157:182–93. https://doi.org/10.1016/j.conbuildmat.2017.09.057.
[22] Naeimi N, Moustafa MA. Numerical modeling and design sensitivity of structural and seismic behavior of UHPC bridge piers. Eng Struct 2020;219:110792. https://doi.org/10.1016/j.engstruct.2020.110792.
[23] Kang ST, Lee Y, Park YD, Kim JK. Tensile fracture properties of an Ultra High Performance Fiber Reinforced Concrete (UHPFRC) with steel fiber. Compos Struct 2010;92:61–71. https://doi.org/10.1016/j.compstruct.2009.06.012.
[24] Zhu Y, Zhang Y, Hussein HH, Chen G. Flexural strengthening of reinforced concrete beams or slabs using ultra-high performance concrete (UHPC): A state of the art review. Eng Struct 2020;205:110035. https://doi.org/10.1016/j.engstruct.2019.110035.
[25] Zhang Y, Cai S, Zhu Y, Fan L, Shao X. Flexural responses of steel-UHPC composite beams under hogging moment. Eng Struct 2020;206:110134. https://doi.org/10.1016/j.engstruct.2019.110134.
[26] Zeng X, Deng K, Liang H, Xu R, Zhao C, Cui B. Uniaxial behavior and constitutive model of reinforcement confined coarse aggregate UHPC. Eng Struct 2020;207:110261. https://doi.org/10.1016/j.engstruct.2020.110261.
[27] Wang Z, Wang J, Zhao G, Zhang J. Design criterion for the self-centering capacity of precast segmental UHPC bridge columns with unbonded post-tensioning tendons. Eng Struct 2019;200:109706. https://doi.org/10.1016/j.engstruct.2019.109706.
[28] Pereiro-Barceló J, Bonet JL, Albiol-Ibáñez JR. Buckling of steel and Ni-Ti reinforcements in very high performance concrete (VHPC) elements. Constr Build Mater 2018;160:551–63. https://doi.org/10.1016/j.conbuildmat.2017.11.113.
[29] Zhang Y, Zhu P, Shi J. Flexural behavior of precast UHPC beam with prestressed bolted hybrid joint. Eng Struct 2020;206:110100. https://doi.org/10.1016/j.engstruct.2019.110100.
[30] Zhang G, Han Q, Xu K, Du X, He W. Experimental investigation of seismic behavior of UHPC-filled socket precast bridge column-foundation connection with shear keys. Eng Struct 2020. https://doi.org/10.1016/j.engstruct.2020.111527.
[31] Saiidi MS, Tazarv M, Nakashoji B, Varela S, Kavianipour F. Resilient and Sustainable Bridges of the Future. Int J Bridg Eng 2015;3:37–48.
[32] Bonet JL, Pereiro-Barceló J, Navarro-Gómez A. Elemento de Conexión de Protección Contra Sismos: P201631022, 2017.
[33] Alam MS, Moni M, Tesfamariam S. Seismic overstrength and ductility of concrete buildings reinforced with superelastic shape memory alloy rebar. Eng Struct 2012;34:8–20. https://doi.org/10.1016/j.engstruct.2011.08.030.
[34] Billah AHMM, Shahria Alam M. Plastic hinge length of shape memory alloy (SMA) reinforced concrete bridge pier. Eng Struct 2016;117:321–31. https://doi.org/10.1016/j.engstruct.2016.02.050.
[35] Billah AHMM, Alam MS. Probabilistic seismic risk assessment of concrete bridge piers reinforced with different types of shape memory alloys. Eng Struct 2018;162:97–108.

https://doi.org/10.1016/j.engstruct.2018.02.034.

[36] Muntasir Billah AHMM, Shahria Alam M. Seismic performance of concrete columns reinforced with hybrid shape memory alloy (SMA) and fiber reinforced polymer (FRP) bars. Constr Build Mater 2012;28:730–42. https://doi.org/10.1016/j.conbuildmat.2011.10.020.

[37] Jiang S, Zhang Y. Microstructure evolution and deformation behavior of as-cast NiTi shape memory alloy under compression. Trans Nonferrous Met Soc China 2012;22:90–6. https://doi.org/10.1016/S1003-6326(11)61145-X.

[38] Qiu CX, Zhu S. Characterization of cyclic properties of superelastic monocrystalline Cu-Al-Be SMA wires for seismic applications. Constr Build Mater 2014;72:219–30. https://doi.org/10.1016/j.conbuildmat.2014.08.065.

[39] Shrestha KC, Saiidi MS, Cruz CA. Advanced materials for control of post-earthquake damage in bridges. Smart Mater Struct 2015;24:25035. https://doi.org/10.1088/0964-1726/24/2/025035.

[40] Mas B, Cladera A, Ribas C. Experimental study on concrete beams reinforced with pseudoelastic Ni-Ti continuous rectangular spiral reinforcement failing in shear. Eng Struct 2016;127:759–68. https://doi.org/10.1016/j.engstruct.2016.09.022.

[41] Pereiro-Barceló J, Bonet JL, Gómez-Portillo S, Castro-Bugallo C. Ductility of high-performance concrete and very-high-performance concrete elements with Ni-Ti reinforcements. Constr Build Mater 2018;175. https://doi.org/10.1016/j.conbuildmat.2018.04.172.

[42] Pereiro-Barceló J, Bonet JL, Cabañero-Escudero B, Martínez-Jaén B. Cyclic behavior of hybrid RC columns using High-Performance Fiber-Reinforced Concrete and Ni-Ti SMA bars in critical regions. Compos Struct 2019;212. https://doi.org/10.1016/j.compstruct.2019.01.029.

[43] Almeida JP de, Steinmetz M, Rigot F, de Cock S. Shape-memory NiTi alloy rebars in flexural-controlled large-scale reinforced concrete walls: Experimental investigation on self-centring and damage limitation. Eng Struct 2020;220:110865. https://doi.org/10.1016/j.engstruct.2020.110865.

[44] Speicher MS, DesRoches R, Leon RT. Experimental results of a NiTi shape memory alloy (SMA)-based recentering beam-column connection. Eng Struct 2011;33:2448–57. https://doi.org/10.1016/j.engstruct.2011.04.018.

[45] Fang C, Zheng Y, Chen J, Yam MCH, Wang W. Superelastic NiTi SMA cables: Thermal-mechanical behavior, hysteretic modelling and seismic application. Eng Struct 2019;183:533–49. https://doi.org/10.1016/j.engstruct.2019.01.049.

[46] Shahverdi M, Czaderski C, Motavalli M. Iron-based shape memory alloys for prestressed near-surface mounted strengthening of reinforced concrete beams. Constr Build Mater 2016;112:28–38. https://doi.org/10.1016/j.conbuildmat.2016.02.174.

[47] Cladera A, Weber B, Leinenbach C, Czaderski C, Shahverdi M, Motavalli M. Iron-based shape memory alloys for civil engineering structures: An overview. Constr Build Mater 2014;63:281–93. https://doi.org/10.1016/j.conbuildmat.2014.04.032.

[48] Hedayati Dezfuli F, Shahria Alam M. Shape memory alloy wire-based smart natural rubber bearing. Smart Mater Struct 2013;22:45013. https://doi.org/10.1088/0964-1726/22/4/045013.

[49] Ruiz-Pinilla JG, Montoya-Coronado LA, Ribas C, Cladera A. Finite element modeling of RC beams externally strengthened with iron-based shape memory alloy (Fe-SMA) strips, including analytical stress-strain curves for Fe-SMA. Eng Struct 2020;223:111152. https://doi.org/10.1016/j.engstruct.2020.111152.

[50] Sutou Y, Omori T, Kainuma R, Ishida K. Ductile Cu–Al–Mn based shape memory alloys: general properties and applications. Mater Sci Technol 2008;24:896–901. https://doi.org/10.1179/174328408X302567.

[51] Pareek S, Suzuki Y, Araki Y, Youssef MA, Meshaly M. Plastic hinge relocation in reinforced concrete beams using Cu-Al-Mn SMA bars. Eng Struct 2018;175:765–75. https://doi.org/10.1016/j.engstruct.2018.08.072.

[52] Hosseini F, Gencturk B, Jain A, Shahzada K. Optimal design of bridge columns constructed with engineered cementitious composites and Cu-Al-Mn superelastic alloys. Eng Struct 2019;198:109531. https://doi.org/10.1016/j.engstruct.2019.109531.

[53] Caballero-Morrison KE, Bonet JL, Navarro-Gregori J, Serna-Ros P. An experimental study of steel fiber-reinforced high-strength concrete slender columns under cyclic loading. Eng Struct

2013;57:565–77. https://doi.org/10.1016/j.engstruct.2012.06.052.
[54] Pereiro-Barceló J, Bonet JL. Mixed model for the analytical determination of critical buckling load of passive reinforcement in compressed RC and FRC elements under monotonic loading. Eng Struct 2017;150. https://doi.org/10.1016/j.engstruct.2017.07.026.
[55] BS EN 1992-1-1. Eurocode 2: Design of concrete structures - Part 1-1 : General rules and rules for buildings. vol. 1. 2004. https://doi.org/[Authority: The European Union Per Regulation 305/2011, Directive 98/34/EC, Directive 2004/18/EC].
[56] AENOR. UNE-EN 12390-3:2020 Ensayos de hormigón endurecido. Parte 3: D... n.d. https://www.une.org/encuentra-tu-norma/busca-tu-norma/norma?c=N0063272 (accessed December 12, 2020).
[57] AENOR. UNE-EN 12390-13:2014 Ensayos de hormigón endurecido. Parte 13:... Aenor 2014. https://www.une.org/encuentra-tu-norma/busca-tu-norma/norma/?c=N0053157 (accessed December 12, 2020).
[58] Certification ASA for S and. UNE-EN 14651:2007. Test method for metallic fibre concrete - Measuring the flexural tensile strength (limit of proportionality (LOP), residual) 2017.
[59] AENOR. UNE-EN 10002-1:2002 Materiales metálicos. Ensayos de tracción.... n.d. https://www.une.org/encuentra-tu-norma/busca-tu-norma/norma/?c=N0027411 (accessed December 12, 2020).
[60] ASTM F2004 - 05(2010) Standard Test Method for Transformation Temperature of Nickel-Titanium Alloys by Thermal Analysis n.d. https://www.astm.org/DATABASE.CART/HISTORICAL/F2004-05R10.htm (accessed December 12, 2020).
[61] ACI Committee 374. Acceptance Criteria for Moment Frames Based on Structural Testing and Commentary. 2005.
[62] FEMA 356. FEMA 356 - Prestandard and commentary for the seismic rehabilitation of buildings , FEDERAL EMERGENCY MANAGEMENT AGENCY. 2000.
[63] FEMA 750. NEHRP (National Earthquake Hazards Reduction Program) Recommended Seismic Provisions for New Buildings and Other Structures (FEMA P-750), 2009 Edition. 2009.
[64] Mo YL, Chan J. Bond and slip of plain rebars in concrete. J Mater Civ Eng 1996;8:208–11. https://doi.org/10.1061/(ASCE)0899-1561(1996)8:4(208).
[65] Verderame GM, De Carlo G, Ricci P, Fabbrocino G. Cyclic bond behaviour of plain bars. Part II: Analytical investigation. Constr Build Mater 2009;23:3512–22. https://doi.org/10.1016/j.conbuildmat.2009.07.001.
[66] Khoury S, Sheikh S. Behavior of normal and high strength confined concrete columns with and without stubs /. 1991.
[67] Paultre P, Légeron F, Mongeau D. Influence of concrete strength and transverse reinforcement yield strength on behavior of high-strength concrete columns. ACI Struct J 2001;98:490–501. https://doi.org/10.14359/10292.
[68] Liu J. Seismic Behaviour of Reinforced Concrete Columns. University of Toronto, 2013.
[69] Ho JCM, Pam HJ. Inelastic design of low-axially loaded high-strength reinforced concrete columns. Eng Struct 2003;25:1083–96. https://doi.org/10.1016/S0141-0296(03)00050-6.
[70] Paultre P, Boucher-Trudeau M, Eid R, Roy N. Behavior of Circular Reinforced-Concrete Columns Confined with Carbon Fiber–Reinforced Polymers under Cyclic Flexure and Constant Axial Load. J Compos Constr 2016;20:04015065. https://doi.org/10.1061/(asce)cc.1943-5614.0000624.
[71] Zhu W, Jia J, Gao J, Zhang F. Experimental study on steel reinforced high-strength concrete columns under cyclic lateral force and constant axial load. Eng Struct 2016;125:191–204. https://doi.org/10.1016/j.engstruct.2016.07.018.